Effect of human passage on transport through an air curtain

Narsing K. Jha[1]† **D. Frank**[1] **L. Darracq**[2] **P. F. Linden**[1]

[1]Department of Applied Mathematics and Theoretical Physics, University of Cambridge, Wilberforce Road, CB3 0WA Cambridge, UK
[2]Department of Mechanical Engineering, Ecole Polytechnique, France

(Received xx; revised xx; accepted xx)

Air curtains are commonly used as separation barriers to reduce heat and mass fluxes across open doors of a building. Although air curtains allow an unhampered passage of humans and vehicles, the effect of this traffic on the air curtain performance is not well understood. We study this problem by conducting small-scale waterbath experiments with fresh water, brine and sugar solutions. As a model of human passage, a vertical cylinder is pulled through a planar jet representing an air curtain and separating two zones at either equal or different densities. Experimental parameters and geometries are chosen appropriately to maintain dynamical similarity to full-scale air curtain installations. For the case of an existing density difference across the door, we find that the conventionally defined sealing effectiveness of an air curtain reduces with increasing cylinder speed and this reduction is independent of the direction of travel of the cylinder. For the iso-density case, we propose a new way to evaluate the performance of an air curtain in terms of the effectiveness, defined as the fraction by which an air curtain reduces the infiltration flow due to the cylinder wake compared to an unprotected door situation. Dye visualisations of the air curtain and the cylinder wake are used to examine the re-establishment process of the planar jet after its disruption by the cylinder. Furthermore, two-dimensional time-resolved particle image velocimetry is used to quantify the temporal variations of exchange flux across the air curtain during the entire process of the cylinder motion.

Key words:

1. Introduction

Buoyancy-driven exchange flows across an open doorway between two zones at different temperatures can result in unnecessary heat losses or enhance the spread of particulate substances with detrimental effects in industrial manufacturing processes or laboratory clean rooms. Moreover, human and vehicular traffic through open doorways is also accompanied by additional transport of heat in their wakes, along with many other undesirable agents such as moisture, air-borne contaminants, odours, insects and microorganisms. For example, in hospitals, air infiltration between rooms can result in the spread of disease or cause extra complications for immunocompromised patients (Beggs 2003; Hoffman *et al.* 1999; Lowbury *et al.* 1971; Adams *et al.* 2011).

Air curtains are commonly used to reduce the heat and mass transfer across doors

† Email address for correspondence: navinnaru88@gmail.com

separating two zones in a building at different or equal temperatures or between the inside and outside of a building. In practice, an air curtain is produced by a fan mounted in a manifold usually above the doorway, which drives the air and thus establishes a downward planar air jet that acts as a virtual barrier. Compared to other separation methods such as vestibules, revolving doors or strip curtains, air curtains have reduced space requirements, are more hygienic and provide the least hindrance to traffic. Under optimal operating conditions, an air curtain can reduce the buoyancy-driven air exchange by about 80% compared to an open doorway.

While turbulent jets are well understood (Rajaratnam 1976), their use as a separation barrier is still being explored. The first fundamental and systematic study on air curtains was carried out by Hayes & Stoecker (1969*a*,*b*). They identified the deflection modulus D_m, defined as the ratio of the jet momentum flux and the pressure difference due to the 'stack effect' associated with the buoyancy difference across the doorway,

$$D_m = \frac{\rho_0 b_0 u_0^2}{gH^2\left(\rho_d - \rho_l\right)} = \frac{\left(\rho_0 Q_0^2/b_0\right)}{gH^2\left(\rho_d - \rho_l\right)} = \frac{Q_0^2}{gb_0H^2\left(\frac{T_0}{T_d} - \frac{T_0}{T_l}\right)}, \tag{1.1}$$

as the key parameter for the performance of an air curtain. Here, u_0, ρ_0, T_0 and Q_0 are the discharge velocity, density, temperature and volumetric discharge per unit nozzle length of the jet at the manifold exit, respectively. We approximate the details of this exit as a two-dimensional nozzle of width b_0. The height of the doorway is denoted by H and g is the acceleration due to the gravity. For a doorway between two zones with different temperatures the subscripts d and l are used to denote the properties of the dense (cold) and light (warm) air, respectively. The value of D_m determines the stability of an air curtain: a curtain is said to be stable if it reaches the opposite side of the doorway, i.e. the floor if directed downwards, and unstable otherwise.

For the case $\rho_l \neq \rho_d$, the performance of an air curtain can be conventionally quantified by the sealing effectiveness E, defined as the fraction of the buoyancy-driven exchange flow prevented by the air curtain compared to the open doorway condition,

$$E \equiv \frac{q - q_{ac}}{q}, \tag{1.2}$$

where q_{ac} and q are the exchange flows through the doorway with and without the air curtain, respectively. A major aim of modelling air curtains is to determine the relationship between E and D_m. Typically, E increases with D_m as a result of disrupting the organised buoyancy-driven flow through the doorway, until a maximum value of E is reached. With further increase in D_m, E decreases. This degradation in performance at higher D_m is caused by mixing across the doorway produced by the air curtain itself (Frank & Linden 2014).

Examining the flow at high D_m, Guyonnaud *et al.* (2000) highlighted the importance of shear layer eddies in the jet and the jet impingement on the floor on the effectiveness E. Sirén (2003*a*,*b*) presented methods for dimensioning an air curtain using momentum and moment-of-momentum balance principles. He also determined the minimum momentum required for the air curtain to reach the opposite side of the doorway, both in the presence and absence of a wind. Sirén (2003*b*) focused on the thermal behavior of the air curtain deriving the expression for the thermal loss and comparing it with empirical results. Full-scale experiments have been performed by Howell & Shibata (1980) and Foster *et al.* (2006), which showed satisfactory agreement with the theoretical predictions of Hayes & Stoecker (1969*b*). Numerical simulations (Costa *et al.* 2006; Foster 2007; Gonçalves *et al.* 2012), a semi-analytical model (Giráldez *et al.* 2013) and laboratory-scale studies

in water (Frank & Linden 2014, 2015) are all in satisfactory agreement with full-scale tests on an air curtain in an otherwise sealed building.

Frank & Linden (2014) studied the effect of an additional ventilation pathway, such as an open window, on the effectiveness of an air curtain and modelled the observed change of performance of the air curtain caused by the resulting change in the neutral level. Frank & Linden (2015) investigated a heated air curtain and observed the reduced stability, effectiveness and energy efficiency of the curtain associated with the opposing buoyancy force. Additionally, wind and pressurised chambers provide external forcing to the air curtain and can destabilise the curtain causing severe oscillations (Havet *et al.* 2003; Rouaud & Havet 2006).

Choi & Edwards (2012) and Tang *et al.* (2013) studied the contaminant transport caused by humans walking through a doorway using large eddy simulation (LES) computations and laboratory experiments, respectively. They examined the effect of a vestibule on the transport and found that a faster walking speed through a vestibule and a larger vestibule results in less mass transport from the contaminated room into the clean room. They also considered the effect of opening various types of doors such as hinged or sliding, and found that the effect of the induced air movement on the human wake had a noticeable effect. Qi *et al.* (2018) studied the effect of a human presence below an air-curtain (but not human passage) and they observed that person had either no influence or reduced the infiltration due to blockage of the doorway.

However, the interaction of humans and their wakes with an air curtain has not been studied and is the motivation for the present work. In this paper, we describe laboratory experiments designed to investigate the effect of human passage on the effectiveness and the stability of an air curtain separating two zones along a corridor in a building. The paper is structured as follows. In §2, we describe the experiments and the techniques used for flow visualization and measurements of the effectiveness and the velocity field. The experimental results are presented in §3. In §3.1, we describe the effect of human passage and the direction of travel on the effectiveness E of an air curtain separating two zones at different temperatures and therefore different densities $\rho_l \neq \rho_d$. In §3.2, we consider the cylinder passage in the iso-density case $\rho_l = \rho_d$ and propose new definitions of the deflection modulus $D_{m,c}$ and the air curtain effectiveness E_c in order to evaluate the performance of an air curtain in that case. We compare the experimental results of §3.1 and §3.2 in §3.3. Dye visualizations of the jet and the infiltration by the wake are described in §3.4. Velocity field measurements from particle image velocimetry (PIV) showing the interaction of the jet and the wake are presented in §3.5 and are used to quantify the temporally varying exchange flux across the air curtain during the entire process of the cylinder motion. Finally, in §4 we summarise our conclusions, provide an overview of how the present study can be helpful for a better design of an air curtain, and discuss strategies for the reduction of the traffic effects on the air curtain effectiveness in practical conditions.

2. Experimental methods

Small-scale waterbath experiments were performed with fresh water and aqueous salt and sugar solutions in a tank with dimensions of length 2 m, width 0.2 m, and depth 0.25 m. The tank, a schematic of which is shown in figure 1, was divided in two equal compartments by a vertical gate, which represented a doorway in a corridor. One side of the tank was filled with water of density ρ_l and the other side with water of density ρ_d, creating a horizontal density difference $\Delta\rho = \rho_d - \rho_l$. The density ratio ρ_l/ρ_d was kept in the range $0.96 - 1$ to maintain the validity of the Boussinesq approximation.

The air curtain device (ACD) consisted of a horizontal cylinder of length 195 mm, closed at the ends, which was fitted across the top of the tank. The cylinder was filled with fine sponge wrapped in a steel wire mesh to uniformly distribute the flow and supplied with fluid of density ρ_0 from an overhead tank. A sequence of 39, 1.0 mm diameter holes separated by 5.0 mm (centre to centre) was drilled along the length of the cylinder, facing downwards on the opposite side to the inlet connections. The circular water jets from the holes merged a few diameters downstream of the nozzle and formed a planar turbulent jet further downstream (Knystautas 1964). The effective planar nozzle width $b_0 = 0.157$ mm was determined as the ratio of total hole area and length of the cylinder.

The air curtain device was placed midway along the length the tank, with the holes on the underside of the cylinder just submerged, and was located near the gate position on the side of the tank with water of density ρ_l (figure 1). In a given experiment the flow rate Q_0, measured by the Omega flow meter (FLR1013), was maintained at a constant value with an accuracy of $\pm 3\%$. In Series A, one value $Q_0 = 425\,\mathrm{mm^2\,s^{-1}}$ was used and in Series B, we used two values $338\,\mathrm{mm^2\,s^{-1}}$ and $480\,\mathrm{mm^2\,s^{-1}}$ (table 1). The turbulence level at the nozzle exit was not measured but Guyonnaud *et al.* (2000) argued that the turbulence intensity does not noticeably affect the air curtain performance.

To represent the passage of a person through an air curtain, a cylinder of diameter $d = 50$ mm and height $l = 170$ mm was pulled at a constant velocity U_c along the centreline of the tank. The base of the cylinder was pulled by a flexible line, attached to a motor via a series of pulleys. To ensure stability during its motion the base of the cylinder consisted of a disc with a larger diameter of 80 mm and height of 15 mm. The speed of the cylinder was controlled by the motor and could be varied in the range of $50 - 250\,\mathrm{mm\,s^{-1}}$. As we discuss below, the height and diameter of the cylinder were chosen to be representative of a typical adult when compared to the height and width of a typical doorway. The velocity of the cylinder was chosen to ensure that the cylinder motion was dynamically similar to human walking. The length of the experimental tank ensured there was an appropriate distance ($\sim 10d$; Honji & Taneda (1969)) to establish the wake of the cylinder before and after its passage through the air curtain.

To facilitate flow visualisation, we used two dye ports injecting dye of different colours. One dye injection point (blue dye) was placed just underneath the nozzle of the air curtain device on the centreline of the tank. The other dye port (red dye) was attached to the front of the cylinder at half the height of the cylinder. A Nikon D3300 camera was used to capture the top and the side-view videos of the experiments at 24 f.p.s. Uniform background illumination was ensured using a projector located 5 m behind the channel and then passing it through a translucent film before entering the tank.

We conducted experiments for two different situations, see table 1. For Series A, the fluid of density ρ_l was fresh water and the fluid of density ρ_d was salt water. The supply to the air curtain was also fresh water, so that in this scenario $\rho_0 = \rho_l < \rho_d$. This arrangement models the situation of a person entering a warm building through an air curtain at the interior building temperature from the cold outside environment. For Series B, the fluid of density ρ_l as well as the initial air curtain supply was sugar water and the fluid of density ρ_d was salt water. For these experiments, we set the densities to be equal, $\rho_0 = \rho_l = \rho_d$, so that there is no buoyancy-driven flow across the doorway and, since molecular diffusion is unimportant in these experiments, the sugar and salt act as passive tracers. This models the case when a person walks through a doorway in an isothermal corridor. All densities were measured using an Anton-Paar density meter DMA 5000 with an accuracy of $7 \times 10^{-3}\,\mathrm{kg\,m^{-3}}$.

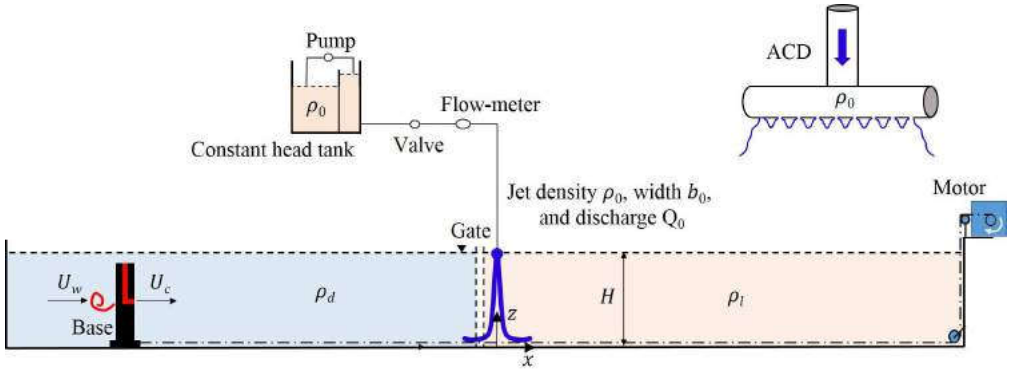

Figure 1: Schematic showing the experimental set-up. Experiments were conducted in a long rectangular tank, each half of which was filled with dense and light fluid of density ρ_d and ρ_l, respectively. Fluid of density ρ_0 was supplied to the air curtain device (ACD) from a constant head tank. A vertical gate was installed beside the curtain to separate the fluid when the air curtain device was switched off. The cylinder was driven by a motor, connected by a flexible thread and a system of pulleys. A dye port injecting red dye was attached to the cylinder to track the wake and the infiltration. Blue coloured dye was injected at the nozzle exit to visualise the air curtain.

Parameter	Definition	Units	Series A	Series B	PIV
Curtain volume flux	Q_0	$\mathrm{mm}^2\,\mathrm{s}^{-1}$	425	338 and 480	480
Mean curtain velocity	$w_m = H/t_{fw}$	$\mathrm{mm\,s}^{-1}$	400	$\sim 300 - 450$	450
Cylinder velocity	U_c/w_m	1	0.16-0.52	0.125-0.625	0.44
Density	ρ_d	$\mathrm{kg\,m}^{-3}$	1002-1041	1400	1000
Density	ρ_l	$\mathrm{kg\,m}^{-3}$	1000	1400	1000
Tracer ρ_d	–	–	Salt	Salt	Fresh water
Tracer ρ_l	–	–	Fresh water	Sugar	Fresh water
Visualisation	–	–	Dye	–	PIV

Table 1: The experimental conditions and parameter values used in experiments. Here, t_{fw} is the time taken by the curtain to reach the bottom of the tank $z/H = 0$ from the cylinder height $z/H \approx 0.85$ in a quiescent environment of the same density, H is the height of the curtain from base of the tank, ρ_l and ρ_d are the densities of the fluid in the dense and light side of the tank, respectively.

2.1. *Series A experiments*

At the beginning of an experiment for Series A, the dense-fluid side ρ_d was filled with salt water up to the height of 210 mm. The water level in the fresh water side was initially set slightly below at 205 mm. The experiment was started by switching on the air curtain device. Once the flow in the jet reached a steady state and the water level in the fresh water side reached the same level as in the salt water side, the vertical barrier between the two compartments was opened and the blue dye port switched on. Subsequently, the cylinder was set into motion at a constant velocity U_c, and the red dye port was opened

to visualise the cylinder wake. The experiments were conducted for different cylinder velocities U_c between $62.5\,\mathrm{mm\,s^{-1}}$ and $210\,\mathrm{mm\,s^{-1}}$. The motor driving the cylinder was stopped when the cylinder reached half distance the between curtain and the opposite end wall of the tank and the vertical gate was immediately closed. We also immediately stopped the flow through the air curtain and closed all the dye ports. The total time t during which the gate was open and allowed the exchange flow (about 10 s) was measured using a stop watch to a precision of 0.1 s. At the end of an experiment, the liquid in the two compartments was fully mixed and the new densities were measured on the light and dense-fluid sides, denoted as ρ_{ln} and ρ_{dn}, respectively. We investigated both directions of travel for the cylinder: from the dense, (equivalently cooler) salt water side (ρ_d) to the lighter, (equivalently warmer) fresh water side (ρ_l) and vice-versa. In the experiments of Series A, we varied the value of the deflection modulus D_m by changing the density ρ_d from $1002 - 1041\,\mathrm{kg\,m^{-3}}$.

Using the mass conservation for the light-fluid half (considering $\rho_0 = \rho_l$), the intruded volume V_i of dense fluid into the light-fluid half during an experimental run was calculated from the measured initial and final densities as

$$V_i = (V_l + \beta q_0 t)\,\frac{(\rho_{ln} - \rho_l)}{(\rho_d - \rho_l)}. \tag{2.1}$$

Here, q_0 is the total source volume flux (in $\mathrm{mm^3\,s^{-1}}$) of the air curtain and V_l is the initial volume of the light-fluid half of the tank. We denote by β the fraction of the air curtain volume flux that spilled into the light-fluid compartment. For our typical jet nozzle volume fluxes $400\,\mathrm{mm^2\,s^{-1}}$ and run-times of less than 15 s, the volume of water added by the curtain to the light-fluid compartment was at most 2% of the total volume if $\beta = 1$. Any value of β between 0.5 and 1 can be chosen with an error of less than 2% of V_i, and we used $\beta = 0.5$. The same formula omitting the correction $\beta q_0 t$ can be used to calculate the intruding volume of dense water V_i into the light-fluid side if the air curtain is not operating.

In order to assess the performance of an air curtain in terms of the effectiveness E as in (1.2), we need to compute q_{ac} and q. For the case of an undisturbed air curtain the definition of the effectiveness given by (1.2) is time-independent. When a cylinder moves through the air curtain, the flux q_{ac} across the doorway is modified by the interaction of the air curtain with the cylinder wake and becomes, in principle, time-dependent. Consequently, in the experiments q_{ac} has an initial steady value before the cylinder passage, which increases while the cylinder moves through the curtain and returns to its initial value after the cylinder has passed. More precisely, the total infiltration flux q_{ac} can be decomposed as

$$q_{ac} = q_{ac,m} + q_{ac,cyl}, \tag{2.2}$$

where $q_{ac,m}$ is the exchange flux caused by the mixing process within the air curtain, assumed to be time-independent, and $q_{ac,cyl}$ is the infiltration flux due to the curtain-wake interaction. In absence, of a moving cylinder, $q_{ac} = q_{ac,m}$.

In our experiments we focus only on the immediate processes associated with the cylinder passage through the air curtain and the time frame when q_{ac} is increased due to the curtain-wake interaction, i.e., $q_{ac,cyl} \neq 0$. While q_{ac} may still vary during this time frame, it is non-trivial to measure this temporal variation. Thus we measure the time-averaged q_{ac} by measuring the densities at the start and the end of an experiment and use (1.2) to calculate this 'cumulative' effectiveness for a cylinder moving a fixed

distance before and after the air curtain. The measured exchange flux q_{ac} when the air curtain is operating is

$$q_{ac} = \frac{V_i}{t}, \tag{2.3}$$

where V_i is given in (2.1) and t is the measured duration of the experiment.

We obtained the reference volume flux q by calculating theoretically the amount of exchanged fluid due to the intruding gravity current when the air curtain is switched off. The theoretical expression for the buoyancy-driven exchange, also known as the orifice equation, is written as

$$q = \frac{1}{3} C_d A \sqrt{g' H}, \tag{2.4}$$

where $g' = g(1 - \rho_l/\rho_d)$ is the reduced gravity, A is the area and H is the height of the opening, respectively. We conducted a series of unobstructed exchange flows and found that the measured discharge coefficient for the present opening configuration was $C_d \approx 0.55 \pm 0.03$, which is close to the 0.6 reported in the literature for sharp openings (Linden 1999*a*). The experimental measurements of C_d are presented in appendix A.

2.2. *Series B experiments*

For Series B, we used the same experimental procedure, except that we replaced the fresh water by aqueous sugar solutions and adjusted the densities to represent an isothermal corridor so that $\rho_0 = \rho_l = \rho_d = 1040 \pm 0.5\ \mathrm{kg\,m^{-3}}$. Here, the cylinder was dragged only from the salt water side (ρ_d) to the sugar water side (ρ_l) with and without the air curtain. Note that for Series B we keep the subscripts "l" and "d" with "l" corresponding to the sugar water side and "d" corresponding to the salt water side. We used a calibrated conductivity probe to measure the salt content C in each half of the tank at the beginning and the end of an experiment. These values were then used to calculate the volume V_i of salt water entering the sugar water side during an experimental run as

$$V_i = V_l \frac{(C_{ln} - C_l)}{(C_d - C_l)}. \tag{2.5}$$

Here, V_l is the initial volume in the sugar water side, C_l and C_d denote the initial salt content in the sugar and salt water side, respectively, and C_{ln} in the salt content in the sugar water side at the end of an experimental run. We note the similarities between (2.1) which is based on the conservation of water mass and (2.5) which invokes the conservation of salt mass. Also, in this case we neglect the correction $\beta q_0 t$ in (2.5) since this correction is smaller than the error associated with the conductivity probe measurements.

The choice $\rho_l = \rho_d$ and the use of two tracers allowed us to quantify the effect of the air curtain on the (passive) contaminant transport. As before, we calculate the exchange flux when the air curtain is operating as

$$q_{ac} = \frac{V_i}{t}, \tag{2.6}$$

with V_i given in (2.5). The exchange flux can be decomposed again using (2.2) with $q_{ac,cyl}$ being due to the interaction of the curtain to the wake and $q_{ac,m}$ being the mixing flux induced by the air curtain.

For experiments of Series B, when the air curtain was switched off, we analogously define the exchange flux between both sides of the tank due to the wake of the moving

cylinder as

$$q_{cyl} = \frac{V_i}{t}, \tag{2.7}$$

where V_i is computed using (2.5). The error in the entrained volume measurement is approximately $\pm 2.5\%$ at the highest cylinder speed and $\pm 10\%$ at the lowest speed.

We point out here that both for Series A and Series B, the exchange flux when the air curtain is operating is denoted by q_{ac}. In the absence of an air curtain, the gravity-driven exchange flux in Series A is q and the flux due to the wake of the moving cylinder in Series B is q_{cyl}.

2.3. *PIV measurements*

In order to gain insight into the instantaneous flow field and thr temporal variation of flux, we conducted measurements using the time-resolved 2D particle image velocimetry (PIV). As we shall see later, the dominant interaction between the air curtain and the cylinder wake is largely unaffected by the presence of the density difference $\Delta\rho = \rho_d - \rho_l$ across the doorway for the range of $\Delta\rho$ of practical interest. Consequently, we restricted the use of PIV to cases with no density difference $\Delta\rho = 0$ (pure water) to avoid the impact of refractive index changes and to provide a better representation for the series B experiments. The velocity field was measured in the streamwise and vertical plane through the axis of the cylinder. A thin vertical light sheet was generated by passing the light from a pair of 300 W xenon arc lamps through a thin slit. The arc lamp was equipped with paraboloidal dichroic reflectors, which produce about 35 W of visible light. The light sheet entered the tank after being reflected from a cold mirror to avoid heating the perspex tank. The flow was seeded with 50 µm diameter particles, which were approximately neutrally buoyant. Particle concentrations were chosen such that each correlation box used in the PIV analysis had 6 to 8 particles to provide good correlations. Images were recorded using an ISVI camera with a full resolution of 12 Mpixel. A Nikon 85 mm lens was used and images were captured at a frame rate of 400 f.p.s. with a resolution of 2048×2048 pixels. Exposure times were kept at 0.8 ms and no streaking of particles was observed. We performed the analysis of the image pairs in the DigiFlow software using a box size of 33×33 pixels. The present PIV measurements are similar to those described in more detail in Olsthoorn & Dalziel (2015).

2.4. *Dynamical similarity and comparison to real-scale air curtains*

In the following, we describe the results in terms of the nondimensional cylinder speed $U^* \equiv U_c/w_m$, where the mean velocity of jet front $w_m \equiv H/t_{fw}$ and t_{fw} is the time taken by the curtain to reach the opposite side i.e., the tank bottom $z/H = 0$, from the cylinder head height $z/H \approx 0.85$, in the absence of any buoyancy effects (z is the vertical coordinate). We measured t_{fw} by tracking the curtain front in the recordings where the blue-dyed air curtain with a flow rate q_0 developed into the fresh water environment. For the value of the ACD flow rate of $q_0 \sim 425\,\mathrm{mm\,s^{-2}}$, w_m is about $400\,\mathrm{mm\,s^{-1}}$. We varied the cylinder speed from $62.5\,\mathrm{mm\,s^{-1}}$ to $210\,\mathrm{mm\,s^{-1}}$, which results in values of U^* from 0.16 to 0.52.

These values are typical for the human passage through a full-scale air curtain. For example, walking at a moderate pace of $1\,\mathrm{m\,s^{-1}} = 3.6\,\mathrm{km\,h^{-1}}$ through a typical air curtain with the speed $w_m \sim 2\,\mathrm{m\,s^{-1}}$, gives $U^* \sim 0.5$. This walking speed is significantly faster than a typical buoyancy-driven flow, e.g. a 5K temperature difference across a 2 m high doorway produces a gravity current with the speed $\approx 0.3\,\mathrm{m\,s^{-1}}$, and so the direction of travel has little impact on the exchange. The cylinder Reynolds numbers $Re \equiv U_c d/\nu$

are in the range 3,100 – 10,500 in our experiments compared with $\sim 50,000$ at full scale. Both the experimental and full scale Reynolds numbers are in the shear-layer transition regime (Williamson 1996), so we expect our results to apply at full scale.

In domestic buildings doorways are typically between twice as wide as the human waist and up to 5 to 6 times wider in non-domestic buildings, and the door width in our experiments was four times wider than the cylinder diameter d. Also, the wake width of the cylinder is around $4d$ at a distance of $5d$ away from the cylinder axis. Usually, the cylinder crosses a length of approximately $5d$ while the curtain is re-establishing.

Finally, we note that the use of aqueous salt solutions to represent buoyancy-driven flows in buildings is a well established technique, that retains dynamic similarity due to the lower viscosity of water compared to air and the ability to obtain larger density differences using salt solutions (see e.g. Linden (1999*b*)).

3. Results

3.1. *Effectiveness measurements in Series A experiments*

The variation of the air curtain effectiveness with the deflection modulus for different cylinder speeds for Series A is shown in figures 2a and 2b for the transits from the dense to the light-fluid side and vice-versa, respectively. Recalling (1.2), the effectiveness is

$$E = \frac{q - q_{ac}}{q} = \frac{q - (q_{ac,m} + q_{ac,cyl})}{q}, \tag{3.1}$$

where we use the decomposition (2.2).

For the base case of the air curtain operating without the cylinder transit, $q_{ac,cyl} = 0$, the effectiveness E first increases with the deflection modulus until it reaches a maximum value of about 0.8 at $D_m \sim 0.2$, and then decreases slowly with further increase in D_m. This value of maximum effectiveness and the dependence on D_m is similar to the values measured previously at a doorway between two rooms by Frank & Linden (2014) and others. This similarity between the present case of a doorway in corridor and doorways between (wider) rooms suggests that the exchange across the doorway is not sensitive to the room configurations and is determined locally at the doorway itself. At the maximum effectiveness, the curtain is stable and impinges on the floor. As mentioned previously, with further increase in D_m, the effectiveness E reduces because of the enhanced mixing between two compartments due to the jet entrainment and impingement at the bottom, i.e., an increasing $q_{ac,m}$.

The dependence of the effectiveness E on D_m is shown in figure 2a for different values of the dimensionless cylinder speeds $U^* \equiv U_c/w_m$. In general, the effectiveness E was reduced by the passage of the cylinder as a result of the increased transport across the doorway in the cylinder wake, $q_{ac,cyl} > 0$, and, for a given value of D_m, the reduction increased with increasing cylinder speed. At small values of the deflection modulus, $D_m \leqslant 0.15$, the air curtain is inherently unstable and, thus, the motion of the cylinder had no noticeable effect on the effectiveness. For deflection modulus $D_m \approx 0.2$ where the effectiveness is maximum, E was reduced by approximately 10% at the highest cylinder velocity. At higher values of the deflection modulus the reduction in E increased with increasing D_m. At $D_m > 1$ the effectiveness was reduced by about 25% compared to the base case for $U^* = 0.22$, and more than 55% for $U^* = 0.43$. This trend will be discussed in §3.3.

In the present experiments with $\Delta\rho/\rho = 0.002 - 0.04$, the velocity of buoyancy-driven flow across the doorway in the absence of curtain and cylinder would be $1/2\sqrt{g'H} = 32.5 - 145\,\mathrm{mm\,s^{-1}}$. However, as we shall see in figure 2, for high $\Delta\rho/\rho$ and thus high

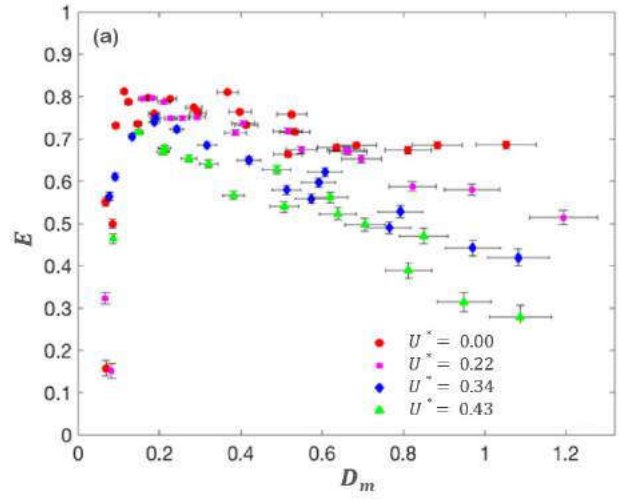

(a)

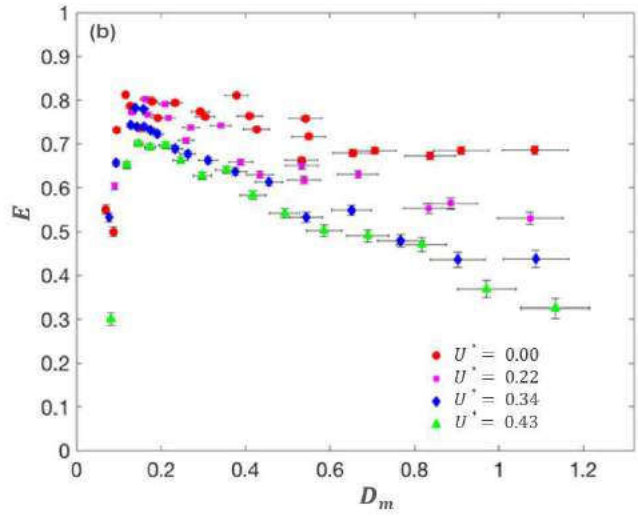

(b)

Figure 2: Air curtain effectiveness E as a function of the deflection modulus D_m for different dimensionless cylinder speeds $U^* \equiv U_c/w_m$: (2a) the cylinder moves from the dense-fluid to the light-fluid side while in (2b) the motion is in the opposite direction. In these experiments the values of the deflection modulus D_m were changed by changing the density difference across the curtain – see (1.1). Consequently, the error bars reflect the uncertainty in the density difference during the course of an experiment.

buoyancy driven flow and low D_m, the buoyancy flux is reduced by 70-80% even in the presence of cylinder, once the curtain is established. Thus, the maximum effective exchange flow velocity will be around 40 mm s^{-1}, which is smaller than cylinder velocity of 62-210 mm s^{-1}. We shall also see later that we observed similar effects using dye visualisation in figure 9, where we observed a noticeable effect of the cylinder passage but little evidence of any buoyancy-driven exchange flow. Consequently, we expect the

direction of the cylinder motion not to play a role, and this is confirmed by the similarity in the data in figures 2a and 2b.

3.2. *Cylinder passage between two iso-density zones in Series B experiments*

In experiments of Series B, we eliminate the buoyancy-driven flow and concentrate on the transport in the cylinder wake. In order to achieve this we used aqueous sugar and salt solutions of the same density on either side of the curtain. Since the molecular diffusion coefficients of salt and sugar are similar and, more importantly, small, the solutes acted as passive tracers and all the transport is either due to the air curtain itself $q_{ac,m}$ or the air curtain and the wake $q_{ac,cyl}$. Such a situation arises, for example, in hospital rooms, where the air curtain can be used to minimize the spreading of airborne infectious substances in the wake of health care professionals walking between isolated hospital rooms.

The Series B experiments can be regarded as the limiting case of the Series A experiments for $D_m \to \infty$. Since there is no significant exchange between two quiescent rooms at the same temperature and an air curtain only introduces such an exchange flow by turbulent mixing, the effectiveness E, defined as in (1.2), for Series B experiments is $E \to -\infty$. Therefore, it is inappropriate to consider the effects of the cylinder on E in these experiments and another method of quantifying these effects needs to be introduced.

For the case of a cylinder moving between two isothermal rooms, we define the new effectiveness

$$E_c = \frac{q_{cyl} - q_{ac}}{q_{cyl}}, \tag{3.2}$$

where q_{cyl} is the exchange flux between two rooms due to the wake of the cylinder moving through an unprotected doorway, i.e., when the air curtain is not operating, as was introduced in (2.7). As before, $q_{ac} = q_{ac,m} + q_{ac,cyl}$ is the exchange flux across the doorway with an air curtain. E_c attains the value of $E_c = 1$ if the air curtain completely prevents the infiltration flow due to the cylinder wake and it assumes the value $E_c = 0$ if the air curtain has no effect on the flow.

The new deflection modulus $D_{m,c}$ is introduced as the ratio of the momentum flux of the air curtain and the lateral momentum flux due to the cylinder motion:

$$D_{m,c} = \frac{b_0 u_0^2}{U_c^2 H} \times \frac{H}{l} \times \frac{W}{d} = \frac{W Q_0^2}{b_0 l d U_c^2}, \tag{3.3}$$

where W is the door width. Large values for $D_{m,c}$ correspond to slow cylinder speeds U_c or to a large air curtain momentum flux. Small values $D_{m,c}$ describe the situation when the cylinder moves fast and the air curtain momentum flux is small. Note that the factors H/l and W/d allow to include the effects of the cylinder geometry in relation to the doorway dimensions. This could be a topic for future investigations but is beyond the scope of the present study.

Figure 3 shows the measured $E_c(D_{m,c})$ curve for experiments of Series B. The data for the $E_c(D_{m,c})$ curve for Series B is less well resolved than the $E(D_m)$ curve for Series A. This is due to the fact that experiments for Series B required a more time-consuming setup which involved matching the densities of sugar and brine solutions.

From figure 3 we can deduce the following pattern for the air curtain effectiveness $E_c(D_{m,c})$: we observe an increase in effectiveness E_c with the deflection modulus $D_{m,c}$ for $D_{m,c} \lesssim 0.2$. The effectiveness E_c reaches its peak value of ≈ 0.4 for $0.2 \lesssim D_{m,c} \lesssim 0.4$. For $D_{m,c} \gtrsim 0.4$, we recognise a slow decrease in the air curtain effectiveness E_c.

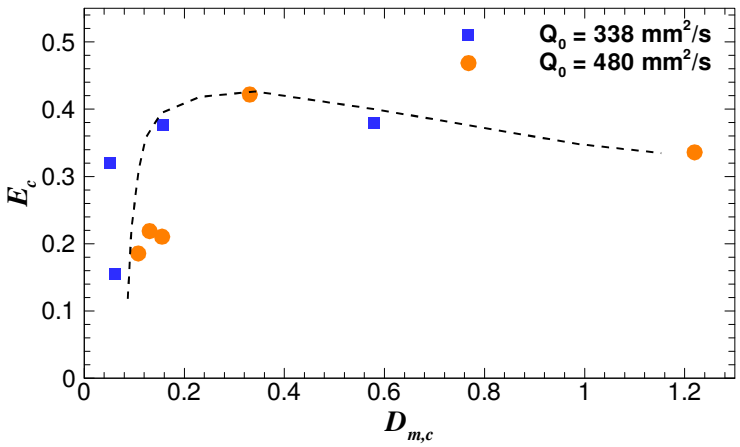

Figure 3: The effectiveness curve $E_c(D_{m,c})$ of the air curtain for Series B experiments, where the effectiveness E_c and the deflection modulus $D_{m,c}$ in the present case of a cylinder moving between two isothermal rooms are defined by (3.2) and (3.3), respectively. The dashed curve is shown to highlight the trend of the data.

3.3. *Comparison and analysis of Series A and Series B experiments*

In the following, we analyse how the results of Series B experiments can be used to better understand the trend of the $E(D_m)$ curves for different U^* (figure 2) of Series A experiments which were discussed in §3.1.

It is instructive to compare the $E_c(D_{m,c})$ curve for the Series B experiments (figure 3) with the $E(D_m)$ curve for Series A experiments when there is no cylinder motion $U^* = 0$ (red dots in figure 2a). Both curves display low and scattered effectiveness values for $D_{m,c} < 0.2$ and $D_m < 0.2$, respectively. For $D_{m,c} > 0.4$ and $D_m > 0.4$ we observe a decrease in E and E_c, which can be attributed to an increasing $q_{ac,m}$ in both cases. However, the peak value $E_c \approx 0.4$ is significantly smaller than the peak value $E \approx 0.8$. The reason for this is that $E(D_m)$ reaches a maximum value when the air curtain completely shields the doorway and the only infiltration flow is due to the entrainment and mixing flux $q_{ac,m}$. For $E_c(D_m)$ curve, in contrast, the air curtain is always temporarily disrupted by the cylinder and $q_{ac,cyl} \neq 0$. We conclude that an optimally operating air curtain is more effective in preventing the stack-pressure driven flux q compared to the equal infiltration flux q_{cyl} associated with the cylinder wake. Similarly, an optimally operating air curtain between two iso-thermal rooms can never reduce the exchange flux q_{cyl} due to the moving cylinder by more than 50%.

If we include the effects of the moving cylinder in Series A, then also the maximum effectiveness E is higher than E_c. This is due to the different reference quantities q and q_{cyl} when the air curtain is not operating that are used in the definitions of E and E_c. For the effectiveness E, the reference value q is the exchange flow associated with the gravity current flow $q = \frac{1}{3} C_d A \sqrt{g' H}$. For E_c, the reference value is the experimentally measured infiltration flux q_{cyl} due to the wake of a moving cylinder. For the range of density differences $\Delta\rho = \rho_d - \rho_l$ and the cylinder speeds U_c used in our experiments, q can be compared to q_{cyl} which is shown in figure 4. For Series A, the deflection modulus value for the maximum effectiveness $D_m \approx 0.2$ is achieved for $\sqrt{g'} \approx 0.37$, for which

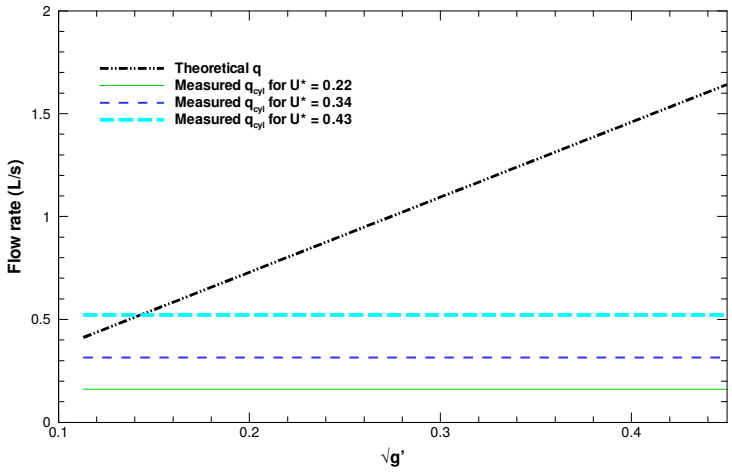

Figure 4: Comparison of the buoyancy-driven exchange flow rate q for the range of $\Delta\rho$ used in our experiments and the infiltration flow rate q_{cyl} due to the moving cylinder for the range of U^* in our experiments. The theoretical line for q was calculated using (2.4). The horizontal lines show the experimentally measured q_{cyl} values for $\Delta\rho = 0$ in Series B. We expand these values as lines across a range of g' for an easier visual comparison between q_{cyl} and q.

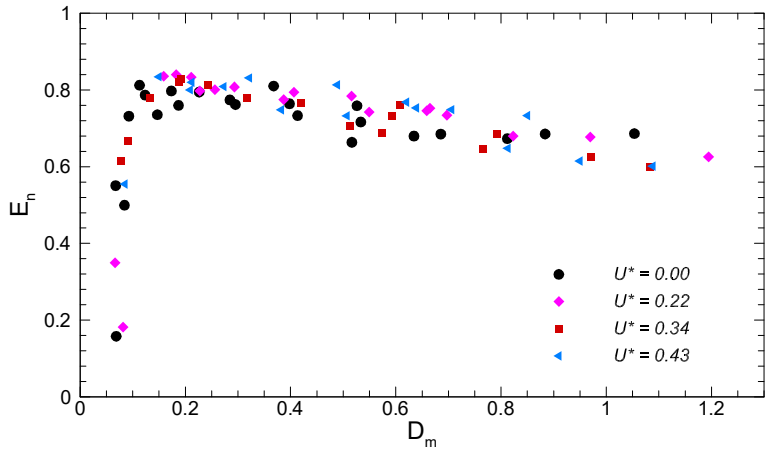

Figure 5: Corrected effectiveness curves $E_n(D_m)$ of an air curtain for different dimensionless cylinder speeds U^* as calculated using (3.5). The corrected effectiveness curves collapse onto the air curtain effectiveness curve for $U^* = 0$, i.e., the case with no moving cylinder.

$q > q_{cyl}$. Thus, the influence of a moving cylinder is only slightly noticeable close to the maximum effectiveness E.

Next, we can use the infiltration fluxes q_{ac} measured in experiments of Series B to better understand the reduction in effectiveness E for $U^* \neq 0$ in experiments of Series A. For Series B experiments ($\Delta\rho = 0$), we conduct one experiment with just an operating air curtain ($Q_0 = 338\,\mathrm{mm^2\,s^{-1}}$) and no moving cylinder, $U^* = 0$. In this particular

experiment, we have $q_{ac,m} = q_{ac}$ since the whole exchange flux between two halves of the tank is only due to the mixing by the air curtain. For $U^* = 0.22,\ 0.34,\ 0.44$ ($Q_0 = 338\,\mathrm{mm^2\,s^{-1}}$) in series B experiments, we can now estimate

$$q_{ac,cyl}\big|_{U^*>0} \approx q_{ac}\big|_{U^*>0} - q_{ac,m}\big|_{U^*=0}. \tag{3.4}$$

Subsequently, we use these $q_{ac,cyl}$ values to calculate the corrected effectiveness values for Series A for $U^* = 0.22,\ 0.34,\ 0.44$ as

$$E_n = E + \frac{q_{ac,cyl}}{q}, \tag{3.5}$$

where E are the effectiveness values presented in figure 2a. The corrected data $E_n(D_m)$ are presented in figure 5. We recognise that when the effectiveness E corrected by $q_{ac,cyl}$ (constant for each U^*), all the $E_n(D_m)$ curves collapse within the experimental error onto the effectiveness curve $E(D_m)$ for $U^* = 0$ (i.e., when there is no moving cylinder). This suggests that there is no strong nonlinear interaction between the wake and the gravity current.

Figure 6 shows the variation of the measured non-dimensionalised q_{ac} flux as a function of the reduced gravity $g' = g\Delta\rho/\rho_l$ for three different U^*. We recognise that once the air curtain is stable $\sqrt{g'} \lesssim 0.37$, the density difference $\Delta\rho$ does not have any influence on the exchange flux q_{ac}. The dots in figure 6 correspond to measurements of Series A and the horizontal lines are each for one data point of Series B experiments. We extend these measurements as horizontal lines to improve the visibility and the comparison with the Series A experiments. There is a small discrepancy between measurements of Series A and Series B experiments for $U^* = 0.22$ (red dots and red line) and for $U^* = 0.43$ (green dots and green line). However, the data is still in the same range and the discrepancy may be attributed to the errors associated with the conductivity probe measurements in Series B experiments.

Figure 4 and figure 6 also reveal why the influence of a moving cylinder is more noticeable for high D_m values in figure 2. In our experiments, we achieve $D_m \to \infty$ by $\Delta\rho \to 0$. In that limit, q becomes small (figure 4) but q_{ac} remains constant (figure 6). Invoking (3.1), the contribution q_{ac}/q increases for an increasing D_m (by reducing $\Delta\rho$), and thus E displays a significant decrease. This provides a simple explanation of the trend of the $E(D_m)$ curves in figure 2 specifically for our experimental arrangement in which we increase D_m by reducing $\Delta\rho$. In the following, we discuss a more general argument for the case when D_m is increased by, for example, increasing the curtain momentum flux $b_0u_0^2$.

We shall assume that the geometric configuration of the doorway and the cylinder is fixed, i.e., the quantities A, H, W, d, l and b_0, which is a reasonable assumption for any real-case scenario. We also consider only the regime in which the air curtain stably impinges on the bottom of the tank. Using (2.4), (1.1) and (3.3) we can re-write the effectiveness E as

(a)

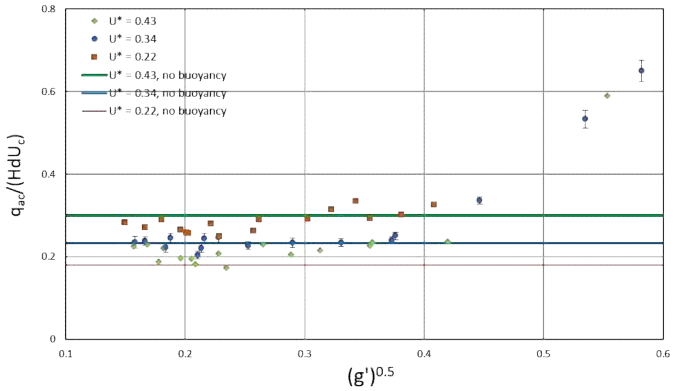

(b)

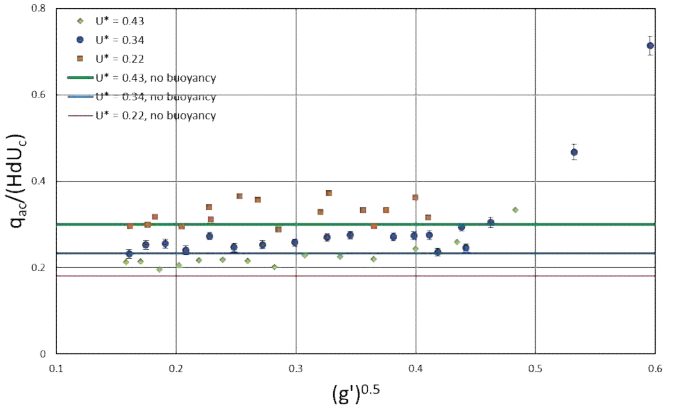

Figure 6: The non-dimensionalised infiltration flow rate $q_{ac}/(HdU_c)$ for an operating air curtain for different cylinder speeds U^* as a function of the non-dimensional horizontal density difference. The direction of the cylinder motion is in (a) from ρ_d to ρ_l and in (b) vice versa. Dots correspond to the measurements of Series A and horizontal lines show the measured values of Series B experiments. Each line corresponds to one data point of Series B experiments which is extended as a horizontal line to improve the visibility and the comparison with the Series A experiments.

$$
\begin{aligned}
E &= 1 - \frac{q_{ac}}{q} \\
&= 1 - \Gamma \cdot \frac{q_{ac}}{W\sqrt{H}\sqrt{g'H^2}} \\
&= 1 - \Gamma \cdot \frac{q_{ac}}{W\sqrt{H}\sqrt{b_0 u_0^2}} \sqrt{D_m} \\
&= 1 - \Gamma \cdot \frac{q_{ac}}{W\sqrt{H}\sqrt{HU_c^2}} \frac{\sqrt{D_m}}{\sqrt{D_{m,c}}} \\
&= 1 - \Gamma \cdot \frac{q_{ac}}{AU_c} \frac{\sqrt{D_m}}{\sqrt{D_{m,c}}},
\end{aligned}
\tag{3.6}
$$

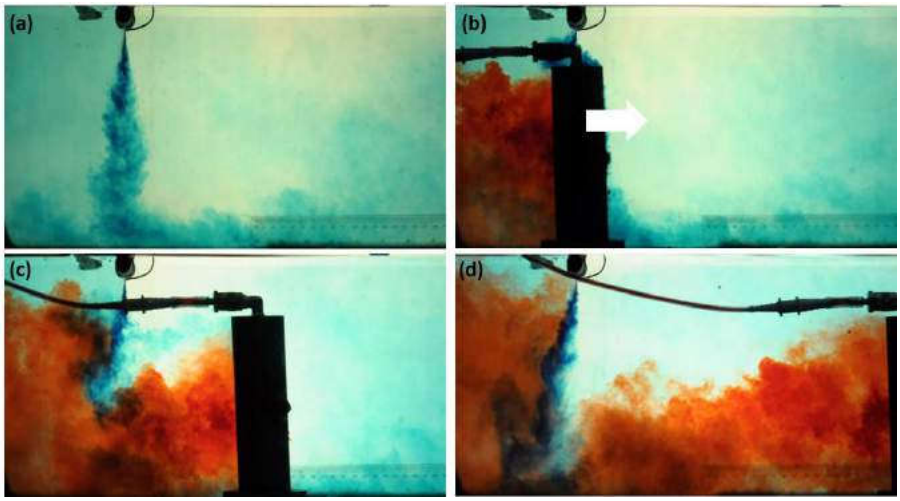

Figure 7: Side views of the interaction between the cylinder and the curtain for $U^* = 0.44$ and $D_m = 0.5$. The cylinder is moving from the dense to the light-fluid side (from left to right as marked in (b)). The blue-dyed curtain jet separates the dense and the light fluid in (a) and the red dye visualises the cylinder wake and the infiltration. The infiltration across the curtain and the re-establishment process is shown in (c). The curtain is re-established in (d).

where $\Gamma > 0$ includes the parameters for the fixed doorway and cylinder geometry and differs from line to line in the previous derivation (but we do not change the notation for the sake of convenience). By further observing

$$U^* = \frac{U_c}{w_m} \sim \frac{U_c}{u_0} \sim \frac{1}{\sqrt{D_{m,c}}} \tag{3.7}$$

we can deduce

$$\begin{aligned} E &= 1 - \Gamma \cdot \frac{q_{ac}}{U_c}\sqrt{D_m}U^* \\ &\approx 1 - \Gamma \cdot \sqrt{D_m}U^*. \end{aligned} \tag{3.8}$$

By going to the last line in (3.8) we make an empirical argument that q_{ac}/U_c is not expected to undergo significant variations for the range of U_c of practical interest. This is demonstrated experimentally in figure 6.

Taking the derivative for a constant $\sqrt{D_m}$

$$\left.\frac{\partial E}{\partial U^*}\right|_{\sqrt{D_m}} \approx -\Gamma \cdot \sqrt{D_m} \tag{3.9}$$

shows that the decrease in E as the consequence of a moving cylinder with speed U^* is more pronounced for large values of D_m. This explains the observed changes in E in figure 2.

3.4. *Dye visualisation and curtain characterisation*

We now present the dye visualisations and use them to further explain the observed flux and effectiveness measurements. Flow visualisation was conducted for three different cylinder speeds and for four different deflection modulus values. The infiltration flux when

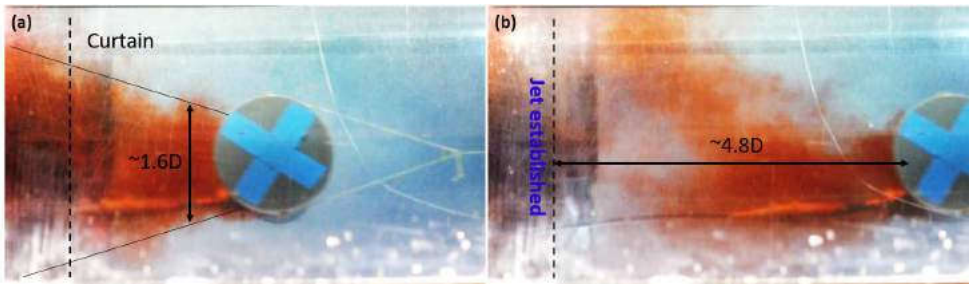

Figure 8: Plan views of the interaction between the cylinder and the curtain for the same parameters as in figure 7, $U^* = 0.44$ and $D_m = 0.5$. The wake expands away from the cylinder and thus the spanwise infiltration across the curtain increases with time. The curtain is re-established in (b). The marked dimensions are in cylinder diameters.

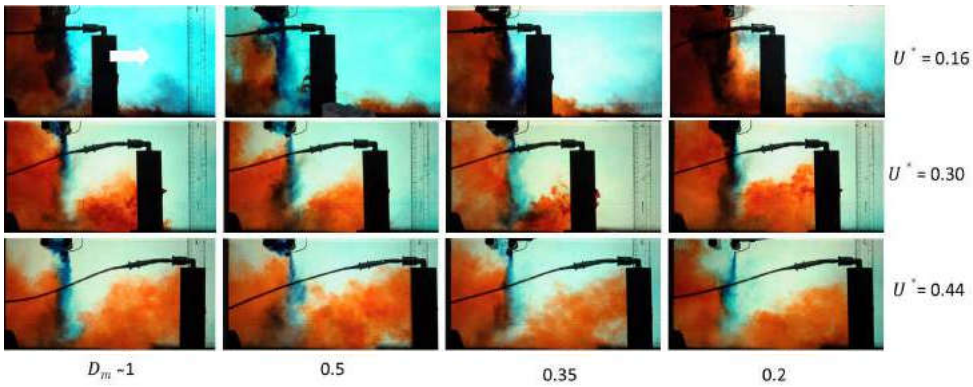

Figure 9: Side views of the cylinder wake and the resulting infiltration when the curtain is first re-established for a range of cylinder speeds and deflection moduli. The cylinder is moving from the dense to the light-fluid side and from left to right in the figure as marked by the white arrow.

the curtain is disrupted is due to the cylinder wake but does not depend significantly on the horizontal density difference $\Delta\rho$ (figure 6). Likewise, the direction of travel does not seem to affect the infiltration flux (figure 2), so we only present the results for the cylinder moving from the dense to the light-fluid side of the tank.

Side views of the passage of the cylinder (left to right, marked by the arrow in figure 7(b)) are shown in figure 7. The cylinder was set into motion 0.6 m away from the air curtain which was not influenced by the cylinder at that distance as can be seen in figure 7(a). As the cylinder approached the air curtain, there was a small deflection of the air curtain in the direction of motion of the cylinder. However, the major disruption occurred as the cylinder passed below the air curtain as shown in figure 7(b). Immediately after the cylinder passed through the air curtain, the infiltration of dense (red) fluid into the light-fluid side took place during the period of re-establishment of the curtain. At later times, the air curtain re-established by penetrating the wake as seen in figure 7(c). Figure 7(d) illustrates the moment when the air curtain was first re-established. A colour movie *'Movie1'* showing the complete infiltration process can be found in the supplementary material.

Plan views of the interaction for the same parameter values are shown in figure 8.

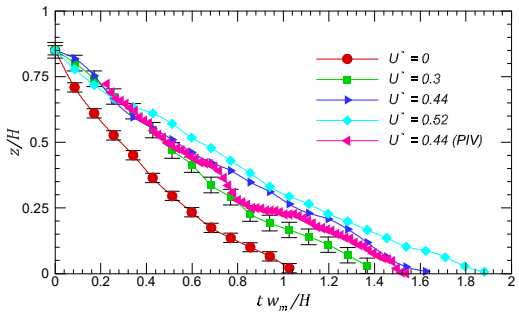

(a) Re-establishment of the curtain as a function of time after the cylinder passage. The front of the curtain is tracked and the time $t = 0$ corresponds to the time when the jet front is at the height of the top of the cylinder, which is $0.15H$ from the nozzle exit. The evolution of the jet is shown for $D_m = 0.5$, $q_0 = 425\,\mathrm{mm}^2\,\mathrm{s}^{-1}$ and for different cylinder speeds $U^* = 0.3$, 0.44, 0.52.

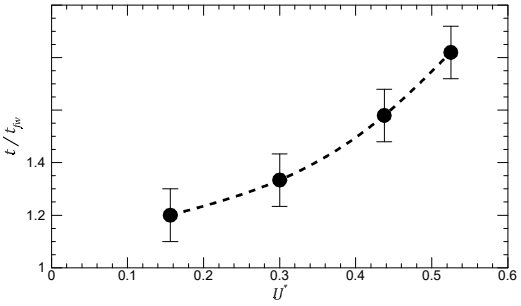

(b) Time taken for the curtain to reach the bottom of the tank for the same experimental parameters as in figure 10a. Here, the time is non-dimensionalised by the time t_{fw} taken for the curtain to reach the tank bottom from the cylinder head in a quiescent fresh water environment.

Figure 10: The curtain re-establishment characteristics for different cylinder speeds. Lines are shown to describe the trends of the data and also to demarcate among different conditions.

As has already been mentioned, the cylinder has a base with a larger diameter, which obscures the view immediately adjacent to the cylinder. The wake width increases with the distance from the cylinder, so that the span-wise width of the infiltration increased with time. In this case the air curtain is re-established (figure 8(b)) after the cylinder has traveled about 5 cylinder diameters beyond the curtain.

Figure 9 shows the disruption and the re-establishment of the air curtain for different cylinder speeds and values of the deflection modulus. These snapshots show the infiltration when the curtain is first re-established. For a given value of the deflection modulus D_m, the amount of the red dyed fluid on the right hand side of the air curtain increases with increasing cylinder speed. This is in line with the experimentally observed decrease in E for a fixed D_m and increasing U^* (figure 2) and the theoretical expectation (3.8). However, there is no noticeable influence of the deflection modulus value, which in the present case is varied by changing $\Delta\rho$, for a fixed U^*. This is to be expected since as shown in figure 6, the flux q_{ac} does not vary significantly with g', and hence, $\Delta\rho$, for a

range of values. We stress, however, that a constant q_{ac} does not imply a constant E, so E will still vary with D_m.

The re-establishment of the air curtain after its disruption determines the total amount of the infiltration by the wake. The dimensionless vertical penetration height z/H of the jet, measured upwards from the tank bottom $z/H = 0$ so that the jet nozzle is at $z/H = 1$, is plotted as a function of time for different cylinder speeds in figure 10a. The measurement for the case $U^* = 0$ was carried out in the fresh water environment without any density difference. This is also the measurement from which we determine t_{fw}. For the other cylinder speeds, we fixed $D_m = 0.5$. We see that the curtain re-establishment time increases with the cylinder speed, presumably a result of the increased momentum in the wake. We will present the detailed results from the PIV in the next subsection. However, here, we briefly present the curtain re-establishment time for $U^* = 0.44$ from the PIV measurements to compare it with the front tracking using dye visualisation in figure 10a. The PIV experiment was conducted in the absence of any buoyancy effects. For PIV, we track the curtain front at 100 f.p.s., taking every fourth frame from the PIV recordings, whereas the front tracking from the dye visualisation is done at 24 f.p.s. In the PIV experiment, the visible bump in the measured curve is due to the presence of a strong eddy near the curtain front. Apart from that, it is very similar to the dye tracking, which includes the presence of buoyancy. This again confirms that the presence of a horizontal density difference $\Delta\rho$ does not significantly affect the curtain interaction with the cylinder wake. The total time required for the curtain to re-establish is plotted in figure 10b. The increasing re-establishment time of the air curtain with the increasing cylinder speed is in line with the measured decrease in its effectiveness.

3.5. *Particle Image Velocimetry*

Two-dimensional PIV measurements in a vertical (x-z) plane along the centreline of the channel were first conducted on the planar turbulent jet in the absence of a cylinder wake to validate the base case flow field. For the mean velocity field, we averaged 2500 instantaneous flow fields captured at 400 f.p.s. at two vertical locations below the nozzle. As seen in figure 11(a), the measurements show that the planar jet was fully developed with very little variation in the mean axial velocity $\overline{w}$ at the two downstream locations. The mean axial velocity $\overline{w}$ profile in this plot is normalized by the mean centreline velocity $\overline{w}_c$ at each location and the lateral distance x from the jet axis is normalized by the distance of half velocity point $x_{\frac{1}{2}m}$. For comparison and validation, the data from Gutmark & Wygnanski (1976) and Heskestad (1965) for the planar turbulent jet are also shown in the figure, with reasonable agreement between their data and ours. The axial turbulent intensity w_{rms} profile, scaled by the axial mean velocity $\overline{w}_c$, is plotted against the lateral distance from the jet axis which is also non-dimensionalised by $x_{\frac{1}{2}m}$ in figure 11(b). The present PIV measurements are found to be in reasonable agreement with the hot-wire data of Gutmark & Wygnanski (1976) and Heskestad (1965).

Two-dimensional PIV measurements will now be presented to examine the velocity field in the vertical plane through the axis of the cylinder during the interaction of the air curtain with the cylinder wake. As we saw in §3.1, the air curtain performance was independent of the direction of the cylinder motion so, as mentioned above, we conducted PIV only for the pure water experiments, Series B. The flow was illuminated with a light sheet that passed through the tank base and some of the light sheet was blocked by the cylinder base. In figure 12, this region is blacked out and the cylinder is marked by horizontal lines. The velocity vectors (u, w) in the $x - z$ plane are represented by arrows,

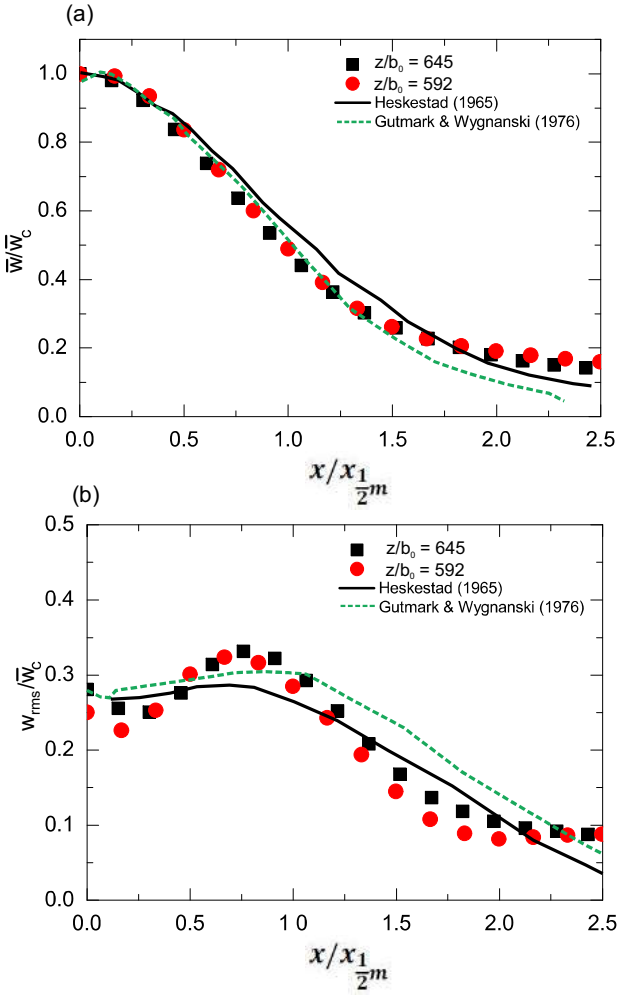

Figure 11: Profiles of the mean and fluctuating vertical (axial) velocity of the turbulent jet produced by the air curtain device in the absence of a cylinder wake measured at two downstream locations $z/b_0 = 592$ and $z/b_0 = 645$. In (a) the profile of the mean axial velocity, normalised by the centreline velocity ($\overline{w}/\overline{w}_c$), is plotted against the normalised lateral distance from the jet axis. In (b), the axial turbulent intensity profile, non-dimensionalised by the mean axial centreline velocity $\overline{w}_c$, is plotted against the normalised lateral distance from the jet axis. For comparison and validation of mean and turbulent properties, the data from Heskestad (1965) and Gutmark & Wygnanski (1976) are also shown, with reasonable agreement between their data and ours.

and the spanwise component of vorticity $\omega_y = w_x - u_z$ is represented by colours. A video of the PIV is provided in the supplementary material as *'Movie2'*.

In the present case, the curtain was naturally turbulent (figure 11(b)) and, when the cylinder was sufficiently far away from the jet, shear layer eddies were visible on both sides of the jet. As the cylinder approached the air curtain (figure 12(a)), the streamwise velocity induced by the cylinder pushes the jet forward. This is in line with our definition of $D_{m,c}$ in (3.3). When the cylinder was closer to the air curtain (figure 12(b)), the central core of the jet was highly perturbed and the shear layer near the cylinder was suppressed.

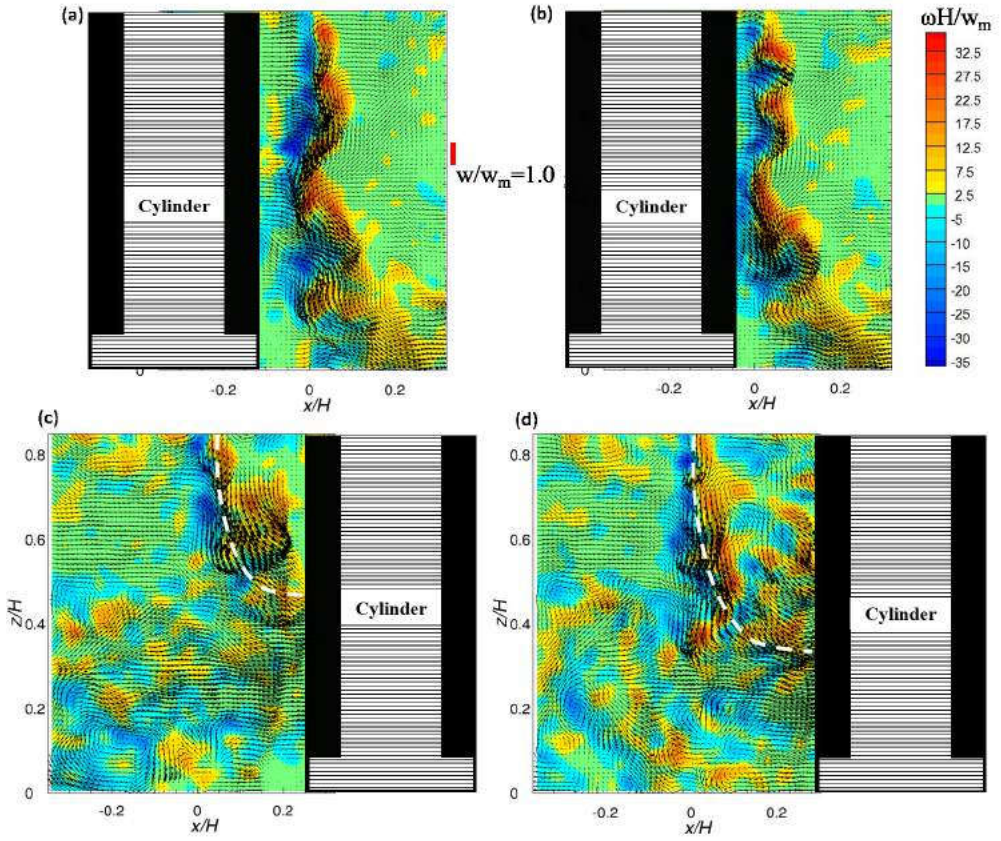

Figure 12: Velocity (arrows) and spanwise vorticity (colours) fields illustrating the passage of the cylinder with speed $U^* = 0.44$ through the air curtain. (a) and (b) shows the distortion of the curtain as the cylinder approaches, and (c) and (d) the flow after the cylinder has passed through the doorway. The black space represents the area where the light is blocked by the cylinder base. The non-dimensional times are (a) $t^* = tw_m/H = -0.69$ and (b) $t^* = tw_m/H = -0.58$. (c) $t^* = tw_m/H = 0.62$ and (d) $t^* = tw_m/H = 0.87$. Similarly to figure 10a, the time $t = 0$ corresponds to the time, when cylinder passes the jet axis. The dimensionless spanwise vorticity ($\omega H/w_m$) is shown beside (b) and the representative length of the velocity vector (w/w_m) is marked beside (a).

The air curtain was completely disrupted when the cylinder was underneath it. After the cylinder passage, the air curtain started to re-establish but the wake velocity continued to pull it towards the cylinder (figure 12(c)). The jet trajectory in figures 12(c) and (d) is shown by the white dotted line. The air curtain started to penetrate the cylinder wake from above and, during this time, an unhindered fluid exchange could take place below the region of the re-establishing air curtain (figure 12(c) and 12(d)). As we saw earlier, the air curtain re-establishment after the cylinder passage was slower than in the quiescent tank. This can be interpreted as being due to the cross-flow forcing of the cylinder wake which interferes with the air curtain. The curtain re-establishment behavior such as its temporal evolution and the re-establishment time is very similar for the PIV and dye measurements as already presented in figure 10a.

In figure 13, we present the meandering of the jet during the re-establishment process.

The interacting vortex is marked by the dashed red line and the jet trajectory is shown by the dashed white line. The induced velocity of the marked vortex is in the clockwise direction in figure 13(a). The jet responds to the velocity induced by these vortical structures and evolves in the direction of the induced velocity. In figure 13(c), a large anti-clockwise vortical structure marked by a magenta ellipse above the establishing jet and a vortex pair marked by the dashed red ellipse can also be observed. The vortex pair induces a strong velocity at the center and the jet is then diverted towards it (figure 13(d)) and the large vortical structure draws it towards the cylinder wake. We have shown in figures 13 the interaction with only two structures whereas, during the re-establishment process, the air curtain interacts in general with many such structures. These are the main cause for the meandering of the jet, which, in turn, produces a higher re-establishment time as seen in figure 10b.

In §2, we discussed that the density measurements allow us to calculate a time-averaged flux q_{ac} when the cylinder motion takes place between two fixed positions before and after the curtain. In particular, we noted that these fixed distances were such that the flux q_{ac} was elevated due to the $q_{ac,cyl}$ contribution through a reasonable fraction of the process of the cylinder motion. The PIV measurements allow us to estimate the temporal variation of q_{ac} and to show that for our choice of the cylinder travel distance, the flux q_{ac} is indeed first elevated due to the interaction of the curtain with the cylinder and then returns back to its original value. As can been seen in figure 14 the flux first increases after $t^* \sim -1$ due to the dynamic pressure of the cylinder (marked as (a) on the figure) as also seen in PIV image in figures 12 (a) and (b). In the time period (b) of figure 14, we observe that flux increases after the passage of the cylinder caused by transport in the wake behind cylinder also seen in PIV image of figure 12 (c). Finally, the flux decreases during period (c), due to the re-establishment of curtain as seen in figure 12 (d).

Figure 14 shows the calculated line flux $\tilde{q}_{ac}/(HU_c)$ from PIV measurements for $U^* = 0.44$ through a vertical line $x/H = 0.08$ where $x = 0$ corresponds to the position of the air curtain device. The time $t^* = tw_m/H$ is normalised by the re-establishment time of the air curtain $t_{fw} = H/w_m$ with $t^* = 0$ chosen as the moment when the cylinder passes directly underneath the air curtain. The time axis covers the entire process of the cylinder motion, from start to finish. We note that our PIV measurements provide a visualisation of the two-dimensional flow field in the streamwise and vertical plane through the axis of the cylinder at the normal coordinate $y = 0$. The dashed line in figure 14 corresponds to the time range when the cylinder passes through the chosen location x/H and the light is blocked by the cylinder base.

To relate the line flux $\tilde{q}_{ac}$ and the (instantaneous) flux q_{ac}, we consider

$$\frac{q_{ac}}{HdU_c} = \frac{\int_{-W/2}^{W/2} \tilde{q}_{ac}(y)dy}{HdU_c}. \tag{3.10}$$

Now, since the interaction of the curtain with the cylinder wake is a three-dimensional process (figures 7 and 8), the line flux $\tilde{q}_{ac}(y)$ will be generally dependent on the normal coordinate y. However, we only have the PIV measurements for the plane $y = 0$. If we make a very crude approximation $\tilde{q}_{ac}(y) \approx \tilde{q}_{ac}(0)$ for $|y| < d/2$ and $\tilde{q}_{ac}(y) \approx 0$ otherwise, then

$$\frac{q_{ac}}{HdU_c} \approx \frac{\tilde{q}_{ac}(y)\big|_{y=0} d}{HdU_c} = \frac{\tilde{q}_{ac}}{HU_c}. \tag{3.11}$$

The mean of the data in figure 14 is $\tilde{q}_{ac}/(HU_c) \sim 0.17$. Comparing it to the data

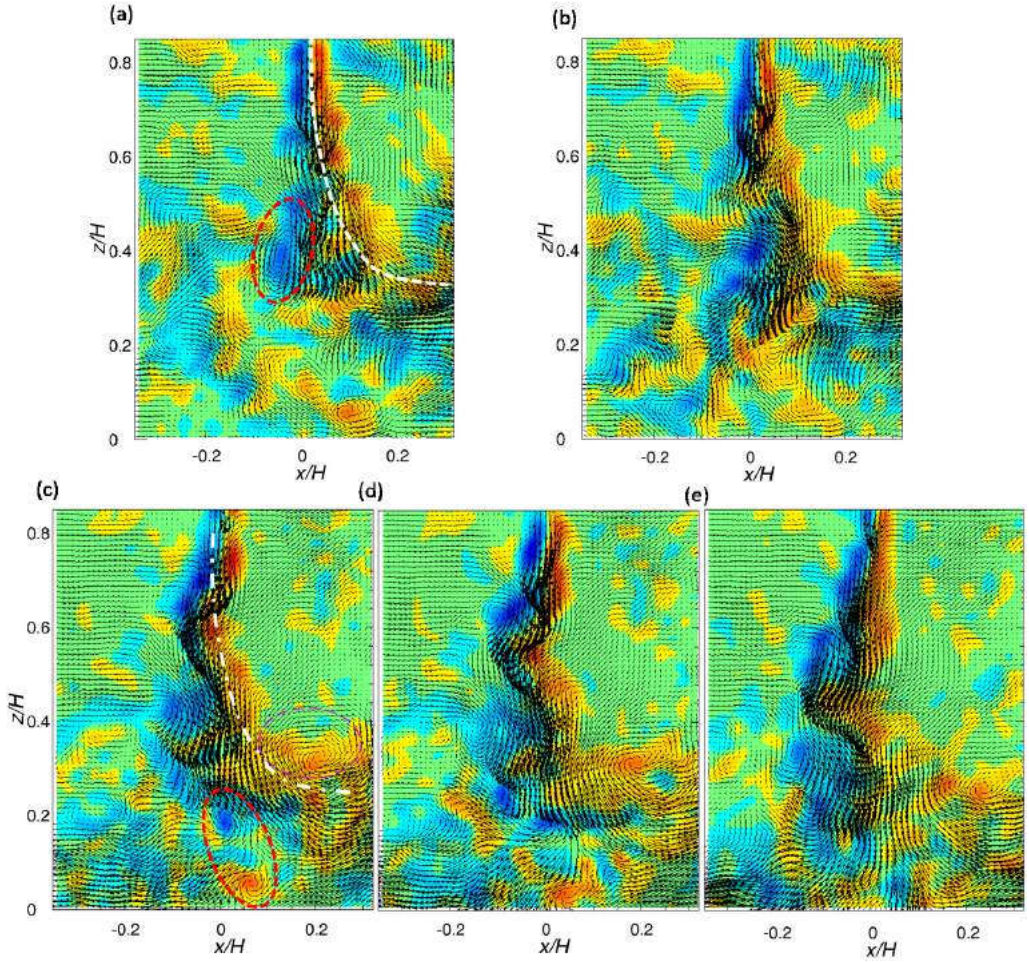

Figure 13: Combined velocity and vorticity fields for a re-establishing curtain after the passage of the cylinder for the same experimental parameters as in figure 12. The white dashed line represents the curtain position. The evolution of the jet is downward and deflected by the cylinder wake as seen in (a). At later times, the jet approaches the tank bottom and is also drawn towards the cylinder. Interaction of the re-establishing jet and the vortex pair is shown further in (c), (d) and (e). The vortex pair is marked by the dashed red line and a single strong vortex by the thin dashed magenta line in (c). The non-dimensional times are (a) $t^* = tw_m/H = 1.10$, (b) $t^* = tw_m/H = 1.26$, (c) $t^* = tw_m/H = 1.95$, (d) $t^* = tw_m/H = 2.04$ and (e) $t^* = tw_m/H = 2.23$.

in figure 6 for $U^* = 0.44$, we observe $q_{ac}/(HdU_c) \sim 0.3$ for Series B (green line) and $q_{ac}/(HdU_c) \sim 0.2$ for Series A experiments (green dots). We already discussed that the discrepancy between the green line and the green dots in figure 6 can be attributed to the error associated with the conductivity probe measurements. Thus, $q_{ac}/(HdU_c)$ can indeed be regarded as an approximation to the average of the temporally varying exchange flux associated with the cylinder motion. The remaining difference in the values is probably due to the exchange occurring over a distance greater than the cylinder diameter in the span-wise direction as also seen in figure 8.

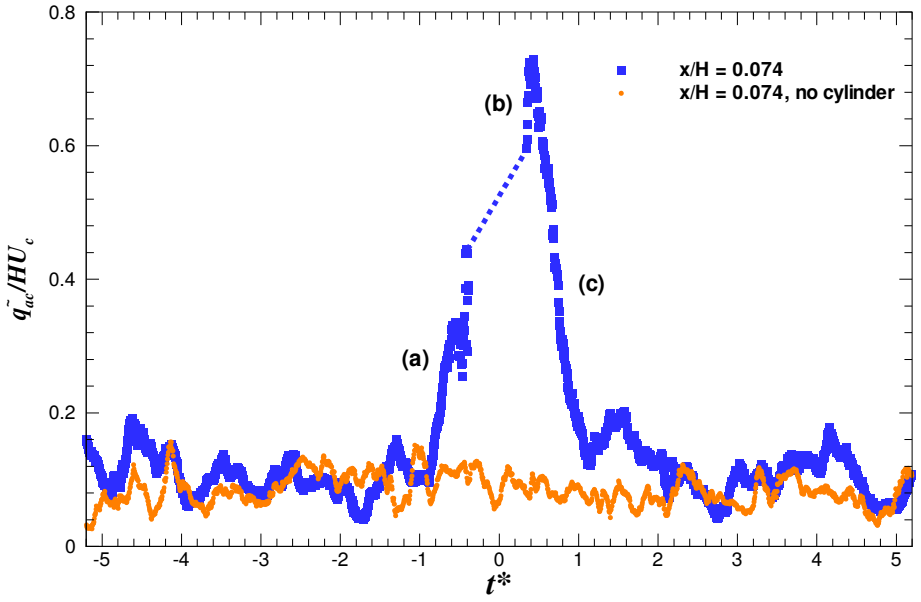

Figure 14: Normalised instantaneous line flux $\tilde{q}_{ac}/(HU_c)$ for the position $x/H = 0.08$ as a function of the normalised time $t^* = t/t_{fw} = tw_m/H$. We choose $t^* = 0$ as the time when the cylinder is directly underneath the air curtain and the time axis extends for the entire process of the cylinder motion. The blue line is plotted for the case $U^* = 0.44$ (the same experiment as in figures 12 and 13) and the orange line shows the reference case of just an air curtain (experiment in figure 11) when there is no cylinder moving across it.

4. Summary and conclusions

We have examined the effect of a cylindrical object, representing a human, passing through the air curtain dividing two zones in a corridor. Small-scale laboratory experiments were conducted using fresh water, salt and sugar solutions, to produce flows dynamically similar to real-scale air curtain installations. We measured the effectiveness $E(D_m)$ curve of an air curtain, separating two enclosures at different temperatures represented by a density difference $\Delta\rho$, with and without the passage of the cylinder, and observed that the effectiveness $E(D_m)$ reduces with increasing cylinder speed U^*. In the absence of traffic, we observed that the air curtain can reduce the contaminant transport by up to about 80% with a stable air curtain, while further increase in the curtain momentum reduces its sealing effectiveness.

For the case of an air curtain separating two isothermal rooms and a cylindrical object moving through the doorway, we established new definitions of the deflection modulus $D_{m,c}$ and the effectiveness E_c. $D_{m,c}$ is based on the momentum flux of the air curtain and the lateral momentum flux due to the cylinder and the effectiveness E_c describes the ability of the air curtain to reduce the flux associated with the wake of the moving cylinder.

Comparison of $E(D_m)$ and $E_c(D_{m,c})$ curves revealed that an air curtain is less effective in preventing the flux due to the cylinder wake than the gravity-driven flux of the same

magnitude. Also, an air curtain can prevent at most half of the contaminant transport in the cylinder wake.

Furthermore, at a fixed deflection modulus D_m, the reduction in E for an increasing U^* can be explained by an increasing infiltration flux due to the disruption of the curtain by the cylinder and the cylinder wake. In particular, this infiltration flux is independent of the horizontal density difference $\Delta\rho$ across the doorway, which suggested that there is no strong interaction between the cylinder wake and the gravity-driven flow. We provided a theoretical argument to explain why the reduction in E is more significant at high values of D_m.

The cylinder disrupts the curtain and visualisations of the jet and the cylinder wake show the infiltration of the fluid carried along with the cylinder wake underneath the unestablished jet is the reason for the observed reduction in the effectiveness. With an increasing cylinder speed, the entrainment in the cylinder wake also increases due to the faster wake velocity which induces a longer time for the re-establishment of the curtain. We also observed that the reduction in effectiveness was independent of the travel direction, because of the faster cylinder speed compared to the stack-driven exchange flow in our experiments and as is typical in most practical situations.

We used the time-resolved two-dimensional particle image velocimetry to study the interaction of the jet and the cylinder wake. We observed that the re-establishment process of the jet is highly unsteady and the jet flaps due to the large vortical structures in the wake leading to an increased mixing across the doorway. These nonlinear interactions lead to an increase in establishment time that is faster than linear in the cylinder velocity. PIV measurements also allowed us to assess the temporal variations of the infiltration flux associated with the transient passage of the cylinder.

We emphasize here that the dimensionless numbers in our experiments were in the same range as for real-scale processes. We varied the deflection modulus D_m from 0 to 1, which is usually the regime achieved by real air curtains (Frank & Linden 2014, 2015). For a person with $l = 1.7\,\mathrm{m}$ and $d = 0.5\,\mathrm{m}$ moving at $U_c = 1\,\mathrm{m\,s^{-1}}$, through a doorway of height $H = 2\,\mathrm{m}$ and width $W = 1\,\mathrm{m}$ and an air curtain discharged from $b_0 = 0.01\,\mathrm{m}$ and a varying outlet velocity $u_0 = 1 - 10\,\mathrm{m\,s^{-1}}$, the $D_{m,c}$ value varies in the range 0.01 and 1.1.

The effect of human passage on the contaminant transport is important in the design and the operation of clean rooms in chemical or pharmaceutical industries and in protecting isolated hospital rooms for infectious and immunocompromised patients from infiltration of air-borne contamination. Our study shows that the human or vehicular traffic reduces the effectiveness. To minimize the air curtain disruption, we suggest a slowing down of the traffic just before the air curtain and then the passage across the air curtain with a much reduced velocity. Also, a higher safety factor on D_m will result in a higher jet velocity, which will help in re-establishing the curtain faster and hence result in a lesser entrainment.

Finally, while the geometry of the channel is directly related to a corridor in a building, as we noted in §3.1, the similarity between the effectiveness as a function of the deflection modulus between these experiments and those conducted in a doorway between two spaces without confining side walls (Frank & Linden 2014) suggests that the exchange is dominated by processes occurring in the immediate vicinity of the doorway, and the geometry of the spaces in either side of the doorway are of secondary importance. Thus we expect our results to hold for a doorway between two rooms or between a room and an unbounded exterior, as is often the case in practice.

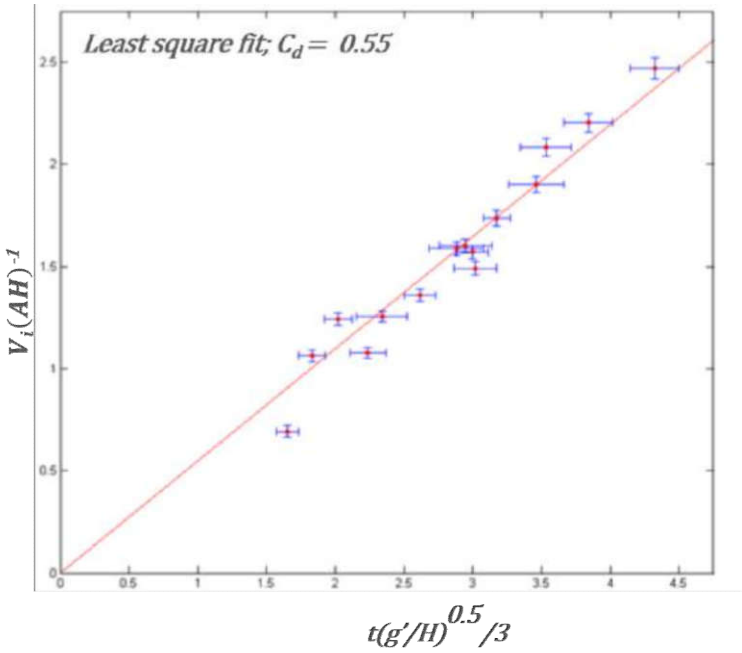

Figure 15: Plot of the non-dimensionalised infiltration volume $V_i\,(AH)^{-1}$ as a function of the non-dimensional time $t\sqrt{g'H^{-1}}/3$ for rectangular channel. Slope of the curve is the discharge co-efficient C_d, which is 0.55±0.03.

Acknowledgements

This research has been supported by the EPSRC through grant EP/K50375/1 and Biddle BV. We would like to thank Prof. Stuart Dalziel and Dr. Jamie Partridge for the discussion and advice during the experiments. We would also like to thank D. Page-Croft for technical support with the experimental setup.

Appendix A. Discharge coefficient

The flux through the doorway in our experiments is proportional to the velocity scale $\sqrt{g'H}$ and the area of the opening (A) by scaling arguments. We opted to represent the proportionality factor as $C_d/3$ (in line with a formula typically used for sharp-edged openings given in (2.4)) and experimentally measured C_d. The proposed model with the measured value of C_d describes the observed flow rate very well. Figure 15 shows the non-dimensional flow rate $V_i\,(AH)^{-1}$ as a function of the non-dimensional time $t\sqrt{g'H^{-1}}/3$ as measured in our experimental setup. The slope of the fitted linear curve is 0.55±0.03, which is the discharge co-efficient C_d. The discharge co-efficient for the sharp opening is also measured, which is 0.59±0.02 as shown in figure 16 and is very close to previously reported value of 0.6.

Appendix B. Supplementary materials

Video caption for supplementary video 1 (Movie1.avi): Temporal evolution of the side view of the interaction using the blue (curtain) and red (cylinder wake) dye for $U^* = 0.44$

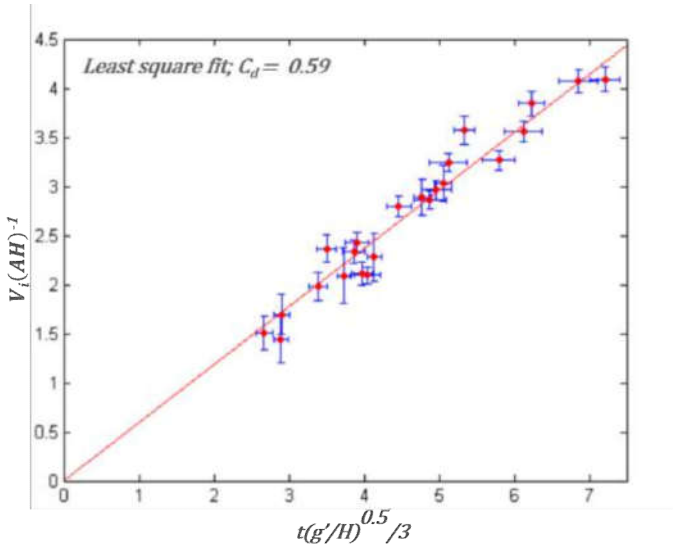

Figure 16: Plot of the non-dimensional volume non-dimensionalised infiltration volume $V_i\,(AH)^{-1}$ as a function of the non-dimensional time $t\sqrt{g'H^{-1}}/3$ for a sharp-edged opening. Slope of the curve is the discharge co-efficient C_d, which is 0.59±0.02.

and $D_m = 0.5$. The cylinder is moving from the dense to the light-fluid side. The video is played at 4.8 times slower than real speed.

Video caption for supplementary video 2 (Movie2.avi): Combined velocity and vorticity field from time resolved PIV measurements of the interaction of the curtain and the cylinder for $U^* = 0.44$ in the absence of any buoyancy effects. The video is played at 16 times slower than real speed. During the cylinder passage, part of the light sheet was blocked by the cylinder base, which can be seen in processed PIV images with mostly zero and few bad velocity vectors in those areas.

REFERENCES

Adams, Noah J, Johnson, David L & Lynch, Robert A 2011 The effect of pressure differential and care provider movement on airborne infectious isolation room containment effectiveness. *American journal of infection control* **39** (2), 91–97.

Beggs, CB 2003 The airborne transmission of infection in hospital buildings: fact or fiction? *Indoor and Built Environment* **12** (1-2), 9–18.

Choi, J-I & Edwards, Jack R 2012 Large-eddy simulation of human-induced contaminant transport in room compartments. *Indoor air* **22** (1), 77–87.

Costa, J. J., Oliveira, L. A. & Silva, M. C. G. 2006 Energy savings by aerodynamic sealing with a downward-blowing plane air curtain - a numerical approach. *Energy and Buildings* **38**, 1182–1193.

Foster, Alan M 2007 Cfd optimization of air movement through doorways in refrigerated rooms. In *Computational Fluid Dynamics in Food Processing*, pp. 167–193. CRC Press.

Foster, A. M., Swain, M. J., Barrett, R., D'Agaro, P. D. & James, S. J. 2006 Effectiveness and optimum jet velocity for a plane jet air curtain used to restrict cold room infiltration. *International Journal of Refrigeration* **29**, 692–699.

Frank, D & Linden, PF 2015 The effects of an opposing buoyancy force on the performance of an air curtain in the doorway of a building. *Energy and Buildings* **96**, 20–29.

Frank, D. & Linden, P. F. 2014 The effectiveness of an air curtain in the doorway of a ventilated building. *Journal of Fluid Mechanics* **756**, 130–164.

Giráldez, H., Segarra, C. D. Pérez, Rodriguez, I. & Oliva, A. 2013 Improved semi-analytical method for air curtains prediction. *Energy and Buildings* **66**, 258–266.

Gonçalves, J. C., Costa, J. J., Figueiredo, A. R. & Lopes, A. M. G. 2012 CFD modelling of aerodynamic sealing by vertical and horizontal air curtains. *Energy and Buildings* **52**, 153–160.

Gutmark, E & Wygnanski, I 1976 The planar turbulent jet. *Journal of Fluid Mechanics* **73** (3), 465–495.

Guyonnaud, L., Solliec, C., de Virel, M. Dufresne & Rey, C. 2000 Design of air curtains used for air confinement in tunnels. *Experiments in Fluids* **28**, 377–384.

Havet, M, Rouaud, O & Solliec, C 2003 Experimental investigations of an air curtain device subjected to external perturbations. *International journal of heat and fluid flow* **24** (6), 928–930.

Hayes, F. C. & Stoecker, W. F. 1969*a* Design data for air curtains. *Transactions of the ASHRAE* **75**, 168–180.

Hayes, F. C. & Stoecker, W. F. 1969*b* Heat transfer characteristics of the air curtain. *Transactions of the ASHRAE* **75 (2)**, 153–167.

Heskestad, Gunnar 1965 Hot-wire measurements in a plane turbulent jet. *Journal of Applied Mechanics* **32** (4), 721–734.

Hoffman, P. N., Bennett, A. M. & Scott, G. M. 1999 Controlling airborne infections. *Journal of Hospital Infection* **43**, 203–210.

Honji, Hiroyuki & Taneda, Sadatoshi 1969 Unsteady flow past a circular cylinder. *Journal of the physical society of Japan* **27** (6), 1668–1677.

Howell, R. H. & Shibata, M. 1980 Optimum heat transfer through turbulent recirculated plane air curtains. *Transactions of the ASHRAE* **2567**, 188–200.

Knystautas, Romas 1964 The turbulent jet from a series of holes in line. *The Aeronautical Quarterly* **15** (1), 1–28.

Linden, Paul F 1999*a* The fluid mechanics of natural ventilation. *Annual review of fluid mechanics* **31** (1), 201–238.

Linden, P. F. 1999*b* The fluid mechanics of natural ventilation. *Annual Review of Fluid Mechanics* **31**, 201–238.

Lowbury, EJL, Babb, JR & Ford, Pamela M 1971 Protective isolation in a burns unit: the use of plastic isolators and air curtains. *Journal of Hygiene* **69** (04), 529–546.

Olsthoorn, Jason & Dalziel, Stuart B 2015 Vortex-ring-induced stratified mixing. *Journal of Fluid Mechanics* **781**, 113–126.

Qi, Dahai, Goubran, Sherif, Wang, Liangzhu Leon & Zmeureanu, Radu 2018 Parametric study of air curtain door aerodynamics performance based on experiments and numerical simulations. *Building and Environment* **129**, 65–73.

Rajaratnam, Nallamuthu 1976 *Turbulent jets*, , vol. 5. Elsevier.

Rouaud, Olivier & Havet, Michel 2006 Behavior of an air curtain subjected to transversal pressure variations. *Journal of environmental engineering* **132** (2), 263–270.

Sirén, K. 2003*a* Technical dimensioning of a vertically upwards blowing air curtain - part i. *Energy and Buildings* **35**, 681–695.

Sirén, K. 2003*b* Technical dimensioning of a vertically upwards blowing air curtain - part ii. *Energy and Buildings* **35**, 697–705.

Tang, Julian W, Nicolle, Andre, Pantelic, Jovan, Klettner, Christian A, Su, Ruikun, Kalliomaki, Petri, Saarinen, Pekka, Koskela, Hannu, Reijula, Kari, Mustakallio, Panu & others 2013 Different types of door-opening motions as contributing factors to containment failures in hospital isolation rooms. *PloS one* **8** (6), e66663.

Williamson, Charles HK 1996 Vortex dynamics in the cylinder wake. *Annual review of fluid mechanics* **28** (1), 477–539.